Photochemical reaction playing a key role in particulate matter pollution over Central France: Insight from the aerosol optical properties

Dawei Hu[1,2*], Ying Chen[3], Yu Wang[2], Véronique Daële[1], Mahmoud Idir[1], Chenjie Yu[2], Jinhe Wang[1,4], Abdelwahid Mellouki[1*]

[1]*Institut de Combustion, Aérothermique, Réactivité et Environnement, ICARE-CNRS/OSUC, Orléans, France*

[2]*School of Earth and Environmental Sciences, University of Manchester, UK.*

[3]*Lancaster Environment Centre (LEC), Lancaster University, UK.*

[4]*School of Municipal and Environmental Engineering, Shandong Jianzhu University, Shandong, China*

**Corresponding authors: dawei.hu@manchester.ac.uk, mellouki@cnrs-orleans.fr*

Abstract

Atmospheric particle is one of the major air pollutants, and believed to be important for air quality, radiative forcing and climate. Measurements of aerosol optical properties, size distribution and PM_{10} concentration were conducted at Orleans, central France during spring (7 March to 25 April) and autumn (25 October to 5 December) 2013. The average values of aerosol scattering coefficient (b_{sca}), absorption coefficient (b_{abs}), single scattering albedo (SSA) at 532 nm and PM_{10} concentration are 54.9 ± 58.2 Mm^{-1}, 10.6 ± 10.9 Mm^{-1}, 0.81 ± 0.10 and 30.6 ± 21.6 $\mu g/m^3$ for the spring campaign, and 35.4 ± 36.7 Mm^{-1}, 3.9 ± 4.4 Mm^{-1}, 0.83 ± 0.13 and 17.4 ± 11.8 $\mu g/m^3$ for the autumn campaign, respectively. During the whole observation, the air parcel transported from Atlantic Ocean plays a role in cleaning up the ambient air in Orleans, while the air mass

coming from the Eastern Europe induces the pollution events in Orleans. In this study, a simple approach, which based on the diurnal variation of PM_{10} concentration, Boundary layer depth (BLD) and the human activity factor derived from anthropogenic emission rate, was introduced to estimate the contribution of secondary aerosol to ambient aerosols. Our results show that secondary particles formation trigged by photochemical reactions and oxidations can contribute maximum of 64% and 32% for PM_{10} mass concentration during the spring and autumn time, respectively. These results highlight that photochemical reactions can enhance the atmospheric oxidation capacity and may faster the secondary particle formation and then play an important role in air quality.

Keywords: Photochemical reactions, Optical properties, Size distribution, Orleans-France, Secondary formation.

Introduction

Atmospheric particles play an important role in affecting air quality, radiative forcing and climate (Charlson et al., 1992). Aerosol particles influence climate both directly, by scattering and absorbing solar and infrared radiation (Charlson et al., 1992;Haywood et al., 1997), and indirectly, by altering the albedo and lifetime of clouds (Kaufman et al., 2005). In addition, the visibility (Vis), as the most readily perceived

impact of air pollution, is highly dependent on the aerosol loading, and can be calculated by aerosol extinction coefficient (b_{ext}), i.e., $Vis=3.912/b_{ext}$ (Seinfeld and Pandis, 2006).

The new particle formation (NPF) and secondary particle (including inorganic and organic) formation processes in the atmosphere can lead to increase of particle number/mass. NPF is one of the main sources of the atmospheric aerosols under the clean environment (such as forest (Makela et al., 1997) and Arctic marine boundary layer (Covert et al., 1996)). Binary nucleation of H_2SO_4-H_2O and ternary H_2SO_4-H_2O-NH_3 were considered as the commonly way for NPF (Seinfeld and Pandis, 2006). Recent study reported that the presence of amine (Kurten et al., 2008;Paasonen et al., 2012;Lv et al., 2015) or organic compounds (Zhang et al., 2004;Schobesberger et al., 2013;Wang et al., 2017) may play an important role in NPF events. NPF can lead to significant increase of ultrafine particle number concentration (Kulmala et al., 2004), however, further studies are needed to quantify its contribution to total particle mass loading. Secondary organic aerosols (SOA) are major contributors to aerosol mass loading, as reported by previous measurements (Zhang et al., 2007;Jimenez et al., 2009;Huang et al., 2014). The common mechanism of SOA formation is the oxidation of volatile organic compounds (VOCs), forming products of lower volatility that subsequently condense to the pre-existing particles. Organic aerosols account for a significant fraction of atmospheric aerosols (Saxena and Hildemann, 1996;Kanakidou

et al., 2005;Zhang et al., 2007). There is growing evidence to show that the organic aerosols, especially SOA particles, play important role in affecting the air quality. On the other hand, secondary inorganic aerosols (SIA), mainly nitrate and sulfate, constitute also a major contributor to particle mass loading, as reported by previous observational (Liu et al., 2017;Wu et al., 2018) and modelling studies (Chen et al., 2016a;Chen et al., 2018). SIA is usually formed from the oxidation of SO_2 and NO_x in heterogeneous reactions (Lelieveld and Heintzenberg, 1992;Riemer et al., 2003;Brown and Stutz, 2012;Chen et al., 2016a;Chen et al., 2018) and gaseous reactions followed by neutralization with ammonia and condense on pre-existing particle surface (Seinfeld and Pandis, 2006). Therefore, the oxidation of VOCs is a critical process of SOA formation, the oxidation of SO_2 and NO_x are an important process of SIA formation.

Photochemical reactions are important source of oxidizing agents in the atmosphere, e.g., ozone and OH radical. Aerosol optical properties are suggested to be good indicators of photochemical reaction events. Aerosol optical properties are believed to be related to their chemical composition. It is well known that light absorption by dust and black carbon aerosols has a warming effect on climate (Jacobson, 2001;Yang et al., 2009;Bond et al., 2013) while light scattering from inorganic aerosols such as sulfate, nitrate, and sea salt has a cooling effect. Field and laboratory studies have reported that the optical properties of organic aerosols are very complex and most

of them exhibit light absorption properties. Chow et al. (2009) observed increasing light absorption toward shorter wavelengths during afternoon hours at the Fresno supersite when the SOA formed by photochemical reactions dominated the total aerosol carbon mass. All those studies suggest that the aerosol absorption related parameters, such as absorption coefficient (b_{abs}) and especially the aerosol concentration independent parameter single scattering albedo (SSA), are good indicators of the atmospheric photochemical reaction events.

In the last decade, aerosol optical properties have been investigated intensively in the world (Table 1), especially in China, but only limited studies were conducted in Europe, and generally those limited works were most concentrated in the Mediterranean area (see Table 1). In March 2014, a heavy pollution episode has occurred in the central interior of France, the observed PM_{10} concentration in Paris was higher than its "alert level", i.e. 80μg/m^3. The central interior of France is under the influence of both polluted air masses from industrial countries (Eastern Europe) and clean ones from Atlantic Ocean (Birmili et al., 2001;Hu et al., 2014). The mixing of these different types of air masses may lead to complex aerosol optical properties in this region. Our previous studies (Hu et al., 2014) have measured the aerosol extinction coefficient in this region (Orleans, France) during autumn time in 2012. The average aerosol extinction coefficient (b_{ext}) at 532 nm measured was 36 ± 31 Mm^{-1}, about 4 times higher than the

values of the air masses from Atlantic Ocean. However, up to now, the knowledge of aerosol optical properties, especially SSA, in the central region of France is very limited. Moreover, the contribution of air masses from Atlantic Ocean and industrial countries (Eastern Europe) to the atmospheric aerosols in the central interior of France is still unclear.

Table 1 Summary of the reported atmospheric aerosol optical property measurement studies.

In this study, aerosol scattering and extinction coefficient were measured in Orleans, a central region of France, during spring and autumn time of 2013. Simultaneous measurements of PM_{10} and gaseous pollutants such as NO_x and O_3 were also conducted during this period. The influences of air masses from Atlantic Ocean and industrial countries on the air quality of the central region of France were explored based on those data and the air masses back trajectory analysis. In addition, the contribution of photochemical reaction process to the atmosphere aerosol mass concentration was estimated according to the data of particle size distribution, boundary layer, human activity factor and PM_{10} concentration.

2. Experimental setup and methods

2.1. Sampling site and period

The measurements presented in this study were made during the period from 7 March to 25 April and from 25 October to 5 December, 2013 at the campus of the Centre National de la Recherche Scientifique (CNRS) in Orleans, France (47°50′16.80″N, 1°56′39.34″E). Orleans city is located in the central France, about 120 km southwest of Paris. The typical average concentrations of O_3, NO_2, NO and PM_{10} from May 2012 to March 2013 in Orleans are 52.8 ± 12.7, 24.0 ± 14.4, 4.3 ± 3.4 and 18.0 ± 5.9 μg/m^3, respectively (http://www.ligair.fr/). Our sampling site, positioned at the CNRS campus, is mostly surrounded by residential dwellings and about 8 km south of the Orleans city center. There are no obstructing buildings around the sampling site within 50 m. During the measurement, Cavity Ring-down Spectrometer (CRDS) and nephelometer (Model 3563, TSI, USA) sampled the ambient aerosols from an inlet located 1 m above the roof of the site (～3.5 m above the ground). Before entering the instruments, the ambient aerosols passed through a 2 m stainless steel tube and a silica drier. In this study, the desiccant was replaced 2 times per week and the relative humidity (RH) of the sample before and after changing the desiccant was monitored for each replacement. The recorded data reveal that the RH of the dehydrated aerosol is less than 15%. Particle number size distribution was also measured by using a scanning mobility particle sizer (SMPS) from 31 October to 9 November, 2013.

2.2. Aerosol Optical Properties

To quantify aerosol optical effects, aerosol optical properties have commonly been determined by measuring scattering coefficient (b_{sca}) using integrated nephelometers (Heintzenberg and Charlson, 1996;Li et al., 2011;Esteve et al., 2012;Li et al., 2013), measuring absorption coefficients (b_{abs}) using the particle/soot absorption photometer (PSAP) (Vrekoussis et al., 2005;Li et al., 2007;Kalivitis et al., 2011), Aethalometer (Hansen et al., 1984;Arnott et al., 2005;He et al., 2009;Kalivitis et al., 2011) and photoacoustic spectrometer (PAS) (Andreae et al., 2008;Garland et al., 2009), as well as measuring extinction coefficient using cavity ring-down spectroscopy (CRDS) (Nakayama et al., 2010;Li et al., 2011;Li et al., 2013;Hu et al., 2014). According to those optical parameters, a useful variable to describe the relative effects of scattering compared with absorption, i.e., single scattering albedo (SSA), can be derived by the equation of $SSA = b_{sca}/b_{ext}$.

In this study, light extinction coefficients of ambient particles were measured using a CRDS at 532 nm. The CRDS system is a self-built and has been described in detail elsewhere (Hu et al., 2014). Briefly, laser light at 532 nm, generated by a pulsed Nd:YAG laser (EXPL-532-200-E, Spectra-Physics Inc., USA), is firstly introduced into a cavity cell and then bounced numerous times between two highly reflective mirrors (532 nm center wavelength, 99.997% reflectivity, 1m radius of curvature, ATFilms Inc.,

USA). Each time the pulse interacts with the back mirror, a small amount of light (e.g., 0.003%) leaks out and is detected by a photomultiplier tube (PMT, R928, Hamamatsu Inc., Japan). After getting the decay time of the cavity filled with (τ) and without (τ_0) aerosols, the aerosol extinction coefficient (b_{ext}) can be calculated according to the following equation:

$$b_{ext} = \frac{L}{cl}\left(\frac{1}{\tau} - \frac{1}{\tau_0}\right) \quad (1)$$

where L is the length between the mirrors (m), l is the effective sample path length (m), c is the speed of light (m/s). During the experiments, the CRDS was operated at the sample flow rate of 2 lpm (liter per minute), resulting a residence time of around 32 s. In addition, in order to avoid interferences from NO_2 and other absorbing trace gas species, blank checks of the CRDS system were performed automatically every 2 h by turning the 3-way valve to the filter direction allowing the measurement of b_{ext} for the particle-free ambient air. Before each measurement, CRDS was calibrated by polystyrene latex spheres (PSL) particles.

Light scattering coefficients of ambient particles were measured using a three-wavelength (450, 550, 700 nm) integrating nephelometer (TSI model 3563, USA). In this study, it was operated at the sample flow rate of 2.5 lpm with a minute averaging time. To avoid the interference of the gas-phase compounds, a 10 min zero check was done automatically by measuring b_{sca} of the particle-free ambient air every 2 h. Before

each field campaign, the nephelometer was calibrated in the laboratory using CO_2 and the filtered air. Due to the design limitations, the scattered light in the nephelometer 3563 was integrated over an angular range of 7-170º, and did not cover the full angular range (0-180º). Thus, a truncation correction developed by Anderson and Ogren (1998) was applied to the measurement data. In addition, to derive the SSA data, the scattering coefficient at 532 nm was calculated by the following equation:

$$b_{sca,532} = b_{sca,\lambda} \times (\frac{532}{\lambda})^{-Å} \quad (2)$$

where the Ångstrom exponent (Å) can be derived from the measurement of $b_{sca,\lambda}$ at two different wavelengths λ_1 and λ_2 through the following equation:

$$Å = -\frac{\log(b_{sca,\lambda_1} / b_{sca,\lambda_2})}{\log(\lambda_1 / \lambda_2)} \quad (3)$$

2.3 Particle Number Size Distribution

The SMPS was described in detail elsewhere (Heim et al., 2004). Herein, only a brief description is presented. In the SMPS system used in this work (TSI Inc., USA), the particles are firstly neutralized with Kr^{85} diffusion charger and size selected using a differential mobility analyzer (DMA, Model 3081). The selected monodisperse particles subsequently go to a butanol-based condensation particle counter (CPC, Model 3022A), which determines the particle concentration at that size. In this study, the detectable aerosol mobility diameters ranged from 10.7 to 487.3 nm with a sheath

and sample flow rates of 5 lpm and 0.5 lpm, respectively. The total counting time required for each sample was about 130 s, consisting of a 120 s up scan and a 10 s retrace. Before measurements, SMPS was calibrated with PSL particles.

2.4 Assessment of secondary particles

In this study, we calculated PM_{10} concentration (PM_{10}_calc) with respect of boundary layer dilution and fresh anthropogenic emissions from human activities (as described in the following) by using equation (4), and compare PM_{10}_calc with the measured PM_{10} concentration (PM_{10}_meas) to investigate the potential influence of secondary particles formation on PM loading.

$$PM_{10_}calc = PM_{10_}meas \times f(\text{anthropogenic emission}) \times f(BLD) \quad (4)$$

where $f(\text{anthropogenic emission})$ is the human activity factor in term of PM emission which was derived from the anthropogenic emission flux of PM at the measurement site, and $f(BLD)$ is the dilution factor of boundary layer change. Both factors are described below in detail.

The anthropogenic emission flux of PM at the measurement site (Kuenen et al., 2014) is presented in Fig S-2. The emission data from TNO (Nederlandse Organisatie voor Toegepast Natuurwetenschappelijk Onderzoek) with consideration of emissions from industry, traffic, residential, agriculture, power and energy and etc. In this study,

we assume the particle loading during the period from 00:00 to 07:00 (local time) is influenced by the anthropogenic emissions (Fig S-1) and photochemical reaction very slightly (PM_{10} concentration was stable during this time period which is showed by the red curves in Fig.2,). While after 07:00, these emissions become stronger and could be a main source of ambient aerosols. To better understand the contribution of anthropogenic emission to the ambient aerosol during the day time, anthropogenic emission flux during 00:00-07:00 were chosen as the reference and normalized to 1, the human activity factor ($f(\text{anthropogenic emission})$) in term of PM emission during the rest hours (07:00-00:00) is calculated as a ratio to the reference value, assuming that the fresh emitted PM is mixed in the boundary layer during the rest hours of the day.

The dilution effect of boundary layer mixing is also considered as following. During the night (00:00-07:00), PM_{10} and Boundary layer depth (BLD) are stable for both campaigns (Fig. 2). The data in this time period are averaged and used as the reference to calculate the variation of PM_{10} concentration which is only due to the dilution effect of boundary layer changing for the remaining hours (07:00-00:00).

3. Results and discussion

3.1 Impact of air mass origination on air quality

Fig. 1 illustrates the b_{ext}, b_{sca}, b_{abs}, SSA at 532 nm, PM_{10}, O_3, NO, NO_2, NO_x, RH and temperature (T) throughout the measurement campaign during the spring time from

7 March to 25 April and during the autumn time from 25 October to 5 December 2013, the corresponding averaged values are summarized in Table 2. The different terms appearing in the second and third rows of Table 2 are further defined and explained in the text. During the whole measurements, the particle optical parameters such as b_{ext}, b_{sca} and b_{abs} are in good agreement with the PM_{10} concentration (R^2 = 0.95, 0.95 and 0.75, respectively). For the spring campaign (Fig. 1(a)), the average values of b_{ext}, b_{sca} and b_{abs} at 532 nm were 65.6 ± 67.8 Mm^{-1}, 54.9 ± 58.2 Mm^{-1} and 10.6 ± 10.9 Mm^{-1}, respectively. This result is comparable with those observed in Eastern and Western Mediterranean (as shown in Table 1), but much lower than those observed in the Mega cities of China (Beijing, Shanghai and Guangzhou) and Japan (Tokyo). During this period, two pollution episodes were observed from 24 March to 1 April (represented as "pollution days", noted as "P-1") and from 2 April to 7 April (noted as "P-2"). The maximum values of PM_{10} and b_{ext} during "P-1" and "P-2" periods reached up to 93.4 $\mu g/m^3$, 317.8 Mm^{-1} and 73.8 $\mu g/m^3$, 249.1 Mm^{-1}, respectively. It is noteworthy that (see Fig. 1(a)) the northeast (NE) wind was dominant during these two pollution events and the air parcel was mainly coming from Eastern Europe (Fig. S-1, calculated by HYSPLIT trajectory model, NOAA, http://ready.arl.noaa.gov/HYSPLIT.php). This result suggests that the air parcel transported from Eastern Europe may be responsible for those two pollution events, a similar event is reported over Germany (Chen et al.,

2016b). As shown in Fig. 1(a), the air quality during the period from 16 March to 19 March (represented as "clean days", noted as "C-1") and from 9 April to 13 April (noted as "C-2") is much better than during the other days. The average PM_{10} and b_{ext} for "C-1" and "C-2" periods are only 10.0 μg/m^3, 23.5 Mm^{-1} and 11.7 μg/m^3, 10.1 Mm^{-1}, respectively. Meteorology (Fig. 1(a)) and air parcel back trajectory (Fig. S-1(a)) reveal that the wind direction during the period of "C-1" and "C-2" was almost southwest (SW), and the air parcel was mainly coming from the Atlantic Ocean. This result is consistent with our previous observations (Hu et al., 2014), i.e. air parcel transported from Atlantic Ocean could improve the air quality of Orleans. In addition, to better understand the influence of air masses from Atlantic Ocean and Eastern Europe on the air quality in Orleans, the period from 20 March to 23 March (noted as "L-1") was selected to represent the local pollution conditions in Orleans since the wind speed is almost zero during this period. As can be seen in Table 2, the average PM_{10} and b_{ext} values during "L-1" period are 30.4 μg/m^3 and 77.9 Mm^{-1}, respectively, about 2.0 and 2.1 times lower than "P-1", 1.5 and 1.7 times lower than "P-2", while about 3.0 and 3.3 times higher than "C-1", 2.6 and 7.7 times higher than "C-2".

Fig. 1. Time series of b_{ext}, b_{sca}, b_{abs}, SSA at 532 nm, PM_{10}, O_3, NO, NO_2, NO_x, RH and T from: (a) 7 March to 25 April, (b) 25 October to 5 December 2013.

Table 2. Summary of the average and maximum values of b_{ext}, b_{sca}, b_{abs}, SSA, PM_{10}, O_3, NO, NO_2 and NO_x during the different period.

For the autumn campaign (Fig. 1(b)), the average values of b_{ext}, b_{sca}, b_{abs} at 532 nm and PM_{10} were 37.5 ± 37.8 Mm^{-1}, 35.4 ± 36.7 Mm^{-1}, 3.9 ± 4.4 Mm^{-1} and 17.4 ± 11.8 $\mu g/m^3$ respectively, about 2 times lower than the values observed during the spring campaign. As shown in Fig. 1(b), the air quality during the period from 25 October to 9 November, represented as "clean days" and noted as "C", was much better than other days. The averages of PM_{10} and b_{ext} during the "C" period were only 3.8 $\mu g/m^3$ and 7.5 Mm^{-1}, respectively. As expected, the SW wind was dominant (Fig. 1(b)) for those clean days and the air parcel was coming from Atlantic Ocean (Fig. S-1(b)). While for other days, from 10 November to 5 December (noted as "M"), the wind direction (Fig. 1(b)) was complex and the air masses came from several different sources (Fig. S-1(b)). The mixing of these different types of air masses can be representative of the typical atmosphere mixing conditions in the Orleans area. As shown in Table 2, the average PM_{10} and b_{ext} values during the "M" period were 22.0 ± 12.7 $\mu g/m^3$ and 52.7 ± 40.5 Mm^{-1}, respectively, about 1.3 and 1.4 times larger than the average values during the whole autumn campaign and 2.2 and 4.3 times larger than during "C" period.

3.2 Diurnal variations of PM_{10}, O_3, NO_x and particles optical properties

Fig. 2 shows the statistic diurnal variation of the PM_{10}, BLD, NO_x, O_3 and photolysis rate of NO_2 (J_{NO2}) during the spring and autumn time. In this "box" diagrams, the mean value is represented by a dot. The dividing segment in the box is the median. The top and bottom box limits represent the 75 and 25 percentile, respectively. The error bars are related to the percentiles 95th and 5th. As shown in Fig 2, the BLD (calculated by Archived Meteorology, GDAS (1 deg. 3hourly. Global), NOAA, http://ready.arl.noaa.gov/READYamet.php) is stable at night while increases consistently in the daytime. The maxima of the average BLD in the daytime are around 1200 and 900 m for the spring and autumn campaigns, respectively, about 5 and 2 times larger than the corresponding night time values. Since the particles concentration is highly influenced by the BLD, the fast increases of BLD in the daytime should decrease the PM_{10} concentration quickly. However, in the real conditions of our measurements (Fig. 2), the daily PM_{10} concentration is stable and only shows a slight decrease during afternoon hours. A reasonable explanation for this phenomenon is that the formed or produced particles from the atmospheric chemical reactions in the daytime may counteract the dilution effect due to the variation of the BLD.

Fig. 2. Statistic diurnal variation of PM_{10}, Boundary layer depth (BLD), NO_x, O_3 and J_{NO2} from: (a) 7 March to 25 April, (b) 25 October to 5 December 2013.

Several field studies have shown that atmospheric photochemical reactions are the main source of atmospheric particles in the daytime. In this study (Fig. 2), a distinct diurnal photochemical reaction process, i.e. strong O_3 formation, was observed in both campaigns. Moreover, there are limited industries in the central region of France and our sampling site is mostly surrounded by residential dwellings, the photochemical reaction processes should be proposed to be the main source of ambient aerosols in Orleans. To further support this point, the statistic diurnal variation of aerosols optical properties (including b_{abs}, b_{sca} and SSA) during the spring and autumn time are present in Fig. 3. In these figures, the SSA exhibits a clear daily pattern, with three "drop down" within a day at 8:00, 14:00 and 18:00 for the spring campaign and at 8:00, 12:00 and 17:00 for the autumn campaign. The daily variability of SSA occurs in the morning, and in the evening is mostly due to the rush hours (Esteve et al., 2012). There is a large amount of black carbon particles emitted during this period. Whereas for the SSA variation occurs in the early afternoon, it is supposed to be derived by the SOA which are formed through photochemical reaction processes because: (1) Field and laboratory studies (Andreae and Gelencser, 2006; Moise et al., 2015) reveal that the organic

aerosols formed by photochemical reactions are another light-absorber in the atmosphere apart from black carbon and mineral dust; (2) the SSA second "drop down" appears at the highest solar intensity (highest J_{NO2}) time. The peak of J_{NO2} is measured at 13:00 and 12:00 within a day for the spring and autumn campaigns, respectively.

Fig. 3. Statistic diurnal variation of b_{abs}, b_{sca} and SSA at 532 nm from: (a) 7 March to 25 April, (b) 25 October to 5 December 2013.

To better understand the impact of photochemical reactions on the air quality in the central region of France, the contribution of photochemical reaction processes to the atmosphere aerosols needs to be estimated. As shown in Fig.2, the PM_{10} and BLD are stable during the night (00:00-07:00) for both campaigns. We assume the variation of PM_{10} concentration is only due to the dilution effect (BLD changes) for the remaining hours (07:00-00:00) and can be calculated according to this stable condition. The difference of PM_{10} between the calculated and measured values can be considered as the contribution of the atmosphere photochemical reaction processes. Actually, this value was overestimated because not only the photochemical reaction processes, but other processes like emissions from human activities can also contribute to the atmospheric aerosol pollution. To avoid the influence of this, the human activity factor

derived from anthropogenic emission rate of $PM_{2.5}$ (from TNO-MACC-II inventory, (Kuenen et al., 2014)) was considered in this work (as shown in Fig. S2). The calculated variation of PM_{10} concentration which considered both BLD dilution and human activities effects is presented as the green curve in Figure 2 (the detailed calculation and parameters was described in part 2.4). Based on the above estimations, the fraction of the photochemical reaction formed particles in PM_{10} was calculated ((PM_{10}_meas – PM_{10}_calc)/ PM_{10}_meas) and presented in Fig.4. It reveals that particles formed from photochemical reactions can account maximum of 64% and 32% for PM_{10} concentration during the spring and autumn times, respectively. These results indicate that photochemical reactions may play an important role in impacting air quality in Orleans.

It is worth to clarify that, in this section, we use the statistical analysis, which based on the data during the whole period in spring or autumn, to show the photochemical reactions can enhance the atmospheric oxidation capacity and may faster the secondary particle formation and then play an important role in air quality. But in section 3.1, we give the case studies to show the air parcel transported from Atlantic Ocean plays a role in cleaning up the ambient air in Orleans, while the air mass coming from the Eastern Europe induces the pollution events in Orleans. Those episodes are occurred with

limited times and short period. The results get from those 2 different analysis methods are not contradictory.

Fig. 4. The estimated fraction of photochemical reaction producing particles in PM_{10}.

3.3. Particles formation and growth events during the typical photochemical reaction process.

To better understand the influence of atmospheric photochemical reaction processes on the air quality in Orleans, the statistic diurnal variation of particles size distribution, NO_x, O_3 and J_{NO2} during the period from 31 October to 9 November, 2013 are presented in Fig. 5. As shown in Fig. 1(b), the air quality is much better during these days. The southwestern wind is dominant during this period and the air parcel comes from Atlantic Ocean (Fig. S-1(b)). This atmospheric meteorological condition is suitable for the observation of new particle formation and growth events since particles transported from Atlantic Ocean are mainly of the micrometer-level (sea salt aerosols). This latter can be easily distinguished with the newly formed nanometer-level particles.

Fig. 5. Statistic diurnal variation of the particle size distribution, NO_x, O_3 and J_{NO2} from 31 October to 9 November, 2013.

As shown in Fig. 5, a clear new particles formation process was observed around 13:00, the maximum particle number concentration reached up to 3488 #/cm^{-3}. As expected, a typical photochemical reaction process with O_3 formation was observed during this period, and O_3 approached its peak value of 60 μg/m^3 (median and mean values) around 13:00. This suggests that photochemical reactions enhance the new particle formation, which may play an important role in impacting air quality in Orleans. Furthermore, the highly humid condition (RH = 92 % in average) during this period also favors the new particle formation process."

4. Conclusions

In this study, the aerosols optical properties, size distribution and PM_{10} concentration measurements were conducted at Orleans, France during spring (7 March to 25 April) and autumn (25 October to 5 December) 2013. The average values of b_{sca}, b_{abs}, SSA at 532 nm and PM_{10} concentration are 54.9 ± 58.2 Mm^{-1}, 10.6 ± 10.9 Mm^{-1}, 0.81 ± 0.10, 30.6 ± 21.6 μg/m^3 and 35.4 ± 36.7 Mm^{-1}, 3.9 ± 4.4 Mm^{-1}, 0.83 ± 0.13, 17.4 ± 11.8 μ/m^3 for the spring and autumn, respectively. During the whole observation, the air parcel transported from Atlantic Ocean plays a role in cleaning up the ambient air

in Orleans, while the air mass coming from the Eastern Europe induces pollution events in Orleans. In addition, a distinct diurnal pattern of photochemical reaction and ozone formation were observed in pollution cases. Further analysis reveals that particles formation triggered by photochemical reactions in daytime can account for a maximum of 64% and 32% of PM_{10} mass loading during the spring and autumn, respectively. Our results highlight that photochemical reactions may play an important role in secondary particles formation and new particles formation and then impacting air quality in the central region of France, and possibly other regions as well.

Acknowledgment

This work was supported by FP7 project (AMIS, No.PIRSES-GA-2011), ARD PIVOTS program (supported by the Centre-Val de Loire regional council), Labex VOLTAIRE (ANR-10-LABX-100-01), the National Natural Science Foundation of China (Nos. 41305124). Dawei Hu thanks Shanghai Tongji Gao Tingyao Environmental Science & Technology Development Foundation for a fellowship support.

References

Anderson, T. L., and Ogren, J. A., 1998. Determining aerosol radiative properties using the TSI 3563 integrating nephelometer. Aerosol Science and Technology. 29, 57-69.

Andreae, M. O., and Gelencser, A., 2006. Black carbon or brown carbon? The nature of light-absorbing carbonaceous aerosols. Atmospheric Chemistry and Physics. 6, 3131-3148.

Andreae, M. O., Schmid, O., Yang, H., Chand, D., Yu, J. Z., Zeng, L. M., et al., 2008. Optical properties and chemical composition of the atmospheric aerosol in urban Guangzhou, China. Atmospheric Environment. 42, 6335-6350.

Arnott, W. P., Hamasha, K., Moosmuller, H., Sheridan, P. J., and Ogren, J. A., 2005. Towards aerosol light-absorption measurements with a 7-wavelength Aethalometer: Evaluation with a photoacoustic instrument and 3-wavelength nephelometer. Aerosol Science and Technology. 39, 17-29.

Birmili, W., Wiedensohler, A., Heintzenberg, J., and Lehmann, K., 2001. Atmospheric particle number size distribution in central Europe: Statistical relations to air masses and meteorology. Journal of Geophysical Research-Atmospheres. 106, 32005-32018.

Bond, T. C., Doherty, S. J., Fahey, D. W., Forster, P. M., Berntsen, T., DeAngelo, B. J., et al., 2013. Bounding the role of black carbon in the climate system: A scientific assessment. Journal of Geophysical Research-Atmospheres. 118, 5380-5552.

Brown, S. S., and Stutz, J., 2012. Nighttime radical observations and chemistry. Chemical Society Reviews. 41, 6405-6447.

Charlson, R. J., Schwartz, S. E., Hales, J. M., Cess, R. D., Coakley, J. A., Hansen, J. E., et al., 1992. Climate forcing by anthropogenic aerosols. Science. 255, 423-430.

Chen, Y., Cheng, Y. F., Ma, N., Wolke, R., Nordmann, S., Schuttauf, S., et al., 2016a. Sea salt emission, transport and influence on size-segregated nitrate simulation: a case study in northwestern Europe by WRF-Chem. Atmospheric Chemistry and Physics. 16, 12081-12097.

Chen, Y., Cheng, Y. F., Nordmann, S., Birmili, W., van der Gon, H., Ma, N., et al., 2016b. Evaluation of the size segregation of elemental carbon (EC) emission in Europe: influence on the simulation of EC long-range transportation. Atmospheric Chemistry and Physics. 16, 1823-1835.

Chen, Y., Wolke, R., Ran, L., Birmili, W., Spindler, G., Schroder, W., et al., 2018. A parameterization of the heterogeneous hydrolysis of N2O5 for mass-based aerosol models: improvement of particulate nitrate prediction. Atmospheric Chemistry and Physics. 18, 673-689.

Chow, J. C., Watson, J. G., Doraiswamy, P., Chen, L. W. A., Sodeman, D. A., Lowenthal, D. H., et al., 2009. Aerosol light absorption, black carbon, and elemental carbon at the Fresno Supersite, California. Atmospheric Research. 93, 874-887.

Covert, D. S., Wiedensohler, A., Aalto, P., Heintzenberg, J., McMurry, P. H., and Leck, C., 1996. Aerosol number size distributions from 3 to 500 nm diameter in the arctic marine boundary layer during summer and autumn. Tellus Series B-Chemical and Physical Meteorology. 48, 197-212.

Esteve, A. R., Estelles, V., Utrillas, M. P., and Martinez-Lozano, J. A., 2012. In-situ integrating nephelometer measurements of the scattering properties of atmospheric aerosols at an urban coastal site in western Mediterranean. Atmospheric Environment. 47, 43-50.

Garland, R. M., Schmid, O., Nowak, A., Achtert, P., Wiedensohler, A., Gunthe, S. S., et al., 2009. Aerosol optical properties observed during Campaign of Air Quality Research in Beijing 2006 (CAREBeijing-2006): Characteristic differences between the inflow and outflow of Beijing city air. Journal of Geophysical Research-Atmospheres. 114.

Hansen, A. D. A., Rosen, H., and Novakov, T., 1984. The aethalometer - an instrument for the real-time measurement of optical-absorption by aerosol-particles. Science of the Total Environment. 36, 191-196.

Haywood, J. M., Roberts, D. L., Slingo, A., Edwards, J. M., and Shine, K. P., 1997. General circulation model calculations of the direct radiative forcing by anthropogenic sulfate and fossil-fuel soot aerosol. Journal of Climate. 10, 1562-1577.

He, X., Li, C. C., Lau, A. K. H., Deng, Z. Z., Mao, J. T., Wang, M. H., et al., 2009. An intensive study of aerosol optical properties in Beijing urban area. Atmospheric Chemistry and Physics. 9, 8903-8915.

Heim, M., Kasper, G., Reischl, G. P., and Gerhart, C., 2004. Performance of a new commercial electrical mobility spectrometer. Aerosol Science and Technology. 38, 3-14.

Heintzenberg, J., and Charlson, R. J., 1996. Design and applications of the integrating nephelometer: A review. Journal of Atmospheric and Oceanic Technology. 13, 987-1000.

Hu, D. W., Li, L., Idir, M., Mellouki, A., Chen, J. M., Daele, V., et al., 2014. Size Distribution and Optical Properties of Ambient Aerosols during Autumn in Orleans, France. Aerosol and Air Quality Research. 14, 744-755.

Huang, R. J., Zhang, Y. L., Bozzetti, C., Ho, K. F., Cao, J. J., Han, Y. M., et al., 2014. High secondary aerosol contribution to particulate pollution during haze events in China. Nature. 514, 218-222.

Jacobson, M. Z., 2001. Strong radiative heating due to the mixing state of black carbon in atmospheric aerosols. Nature. 409, 695-697.

Jimenez, J. L., Canagaratna, M. R., Donahue, N. M., Prevot, A. S. H., Zhang, Q., Kroll, J. H., et al., 2009. Evolution of Organic Aerosols in the Atmosphere. Science. 326, 1525-1529.

Kalivitis, N., Bougiatioti, A., Kouvarakis, G., and Mihalopoulos, N., 2011. Long term measurements of atmospheric aerosol optical properties in the Eastern Mediterranean. Atmospheric Research. 102, 351-357.

Kanakidou, M., Seinfeld, J. H., Pandis, S. N., Barnes, I., Dentener, F. J., Facchini, M. C., et al., 2005. Organic aerosol and global climate modelling: a review. Atmospheric Chemistry and Physics. 5, 1053-1123.

Kaufman, Y. J., Koren, I., Remer, L. A., Rosenfeld, D., and Rudich, Y., 2005. The effect of smoke, dust, and pollution aerosol on shallow cloud development over the Atlantic Ocean. Proceedings of the National Academy of Sciences of the United States of America. 102, 11207-11212.

Kuenen, J. J. P., Visschedijk, A. J. H., Jozwicka, M., and van der Gon, H., 2014. TNO-MACC_II emission inventory; a multi-year (2003-2009) consistent high-resolution European emission inventory for air quality modelling. Atmospheric Chemistry and Physics. 14, 10963-10976.

Kulmala, M., Vehkamaki, H., Petaja, T., Dal Maso, M., Lauri, A., Kerminen, V. M., et al., 2004. Formation and growth rates of ultrafine atmospheric particles: a review of observations. Journal of Aerosol Science. 35, 143-176.

Kurten, T., Loukonen, V., Vehkamaki, H., and Kulmala, M., 2008. Amines are likely to enhance neutral and ion-induced sulfuric acid-water nucleation in the atmosphere more effectively than ammonia. Atmospheric Chemistry and Physics. 8, 4095-4103.

Lelieveld, J., and Heintzenberg, J., 1992. Sulfate cooling effect on climate through in-cloud oxidation of anthropogenic SO2. Science. 258, 117-120.

Li, C., Marufu, L. T., Dickerson, R. R., Li, Z. Q., Wen, T. X., Wang, Y. S., et al., 2007. In situ measurements of trace gases and aerosol optical properties at a rural site in northern China during East Asian Study of Tropospheric Aerosols: An International Regional Experiment 2005. Journal of Geophysical Research-Atmospheres. 112.

Li, L., Chen, J. M., Chen, H., Yang, X., Tang, Y., and Zhang, R. Y., 2011. Monitoring optical properties of aerosols with cavity ring-down spectroscopy. Journal of Aerosol Science. 42, 277-284.

Li, L., Chen, J. M., Wang, L., Melluki, W., and Zhou, H. R., 2013. Aerosol single scattering albedo affected by chemical composition: An investigation using CRDS combined with MARGA. Atmospheric Research. 124, 149-157.

Li, R., Hu, Y. J., Li, L., Fu, H. B., and Chen, J. M., 2017. Real-time aerosol optical properties, morphology and mixing states under clear, haze and fog episodes in the summer of urban Beijing. Atmospheric Chemistry and Physics. 17, 5079-5093.

Liu, Y. C., Wu, Z. J., Wang, Y., Xiao, Y., Gu, F. T., Zheng, J., et al., 2017. Submicrometer Particles Are in the Liquid State during Heavy Haze Episodes in the Urban Atmosphere of Beijing, China. Environmental Science & Technology Letters. 4, 427-432.

Lv, S. S., Miao, S. K., Ma, Y., Zhang, M. M., Wen, Y., Wang, C. Y., et al., 2015. Properties and Atmospheric Implication of Methylamine Sulfuric Acid-Water Clusters. Journal of Physical Chemistry A. 119, 8657-8666.

Makela, J. M., Aalto, P., Jokinen, V., Pohja, T., Nissinen, A., Palmroth, S., et al., 1997. Observations of ultrafine aerosol particle formation and growth in boreal forest. Geophysical Research Letters. 24, 1219-1222.

Moise, T., Flores, J. M., and Rudich, Y., 2015. Optical Properties of Secondary Organic Aerosols and Their Changes by Chemical Processes. Chemical Reviews. 115, 4400-4439.

Nakayama, T., Hagino, R., Matsumi, Y., Sakamoto, Y., Kawasaki, M., Yamazaki, A., et al., 2010. Measurements of aerosol optical properties in central Tokyo during summertime using cavity ring-down spectroscopy: Comparison with conventional techniques. Atmospheric Environment. 44, 3034-3042.

Paasonen, P., Olenius, T., Kupiainen, O., Kurten, T., Petaja, T., Birmili, W., et al., 2012. On the formation of sulphuric acid - amine clusters in varying atmospheric conditions and its influence on atmospheric new particle formation. Atmospheric Chemistry and Physics. 12, 9113-9133.

Riemer, N., Vogel, H., Vogel, B., Schell, B., Ackermann, I., Kessler, C., et al., 2003. Impact of the heterogeneous hydrolysis of N2O5 on chemistry and nitrate aerosol formation in the lower troposphere under photosmog conditions. Journal of Geophysical Research-Atmospheres. 108.

Saxena, P., and Hildemann, L. M., 1996. Water-soluble organics in atmospheric particles: A critical review of the literature and application of thermodynamics to identify candidate compounds. Journal of Atmospheric Chemistry. 24, 57-109.

Schobesberger, S., Junninen, H., Bianchi, F., Lonn, G., Ehn, M., Lehtipalo, K., et al., 2013. Molecular understanding of atmospheric particle formation from sulfuric acid

and large oxidized organic molecules. Proceedings of the National Academy of Sciences of the United States of America. 110, 17223-17228.

Seinfeld, J. H., and Pandis, S. N.: Atmospheric Chemistry and Physics: From Air Pollution to Climate Change, John Wiley & Sons, New York., 2006.

Tang, Y., Huang, Y. L., Li, L., Chen, H., Chen, J. M., Yang, X., et al., 2014. Characterization of aerosol optical properties, chemical composition and mixing states in the winter season in Shanghai, China. Journal of Environmental Sciences. 26, 2412-2422.

Thompson, J. E., Hayes, P. L., Jimenez, J. L., Adachi, K., Zhang, X. L., Liu, J. M., et al., 2012. Aerosol optical properties at Pasadena, CA during CalNex 2010. Atmospheric Environment. 55, 190-200.

Vrekoussis, M., Liakakou, E., Kocak, M., Kubilay, N., Oikonomou, K., Sciare, J., et al., 2005. Seasonal variability of optical properties of aerosols in the Eastern Mediterranean. Atmospheric Environment. 39, 7083-7094.

Wang, Z. B., Wu, Z. J., Yue, D. L., Shang, D. J., Guo, S., Sun, J. Y., et al., 2017. New particle formation in China: Current knowledge and further directions. Science of the Total Environment. 577, 258-266.

Wu, Z. J., Wang, Y., Tan, T. Y., Zhu, Y. S., Li, M. R., Shang, D. J., et al., 2018. Aerosol Liquid Water Driven by Anthropogenic Inorganic Salts: Implying Its Key Role in Haze Formation over the North China Plain. Environmental Science & Technology Letters. 5, 160-166.

Yang, M., Howell, S. G., Zhuang, J., and Huebert, B. J., 2009. Attribution of aerosol light absorption to black carbon, brown carbon, and dust in China - interpretations of

atmospheric measurements during EAST-AIRE. Atmospheric Chemistry and Physics. 9, 2035-2050.

Zhang, Q., Jimenez, J. L., Canagaratna, M. R., Allan, J. D., Coe, H., Ulbrich, I., et al., 2007. Ubiquity and dominance of oxygenated species in organic aerosols in anthropogenically-influenced Northern Hemisphere midlatitudes. Geophysical Research Letters. 34.

Zhang, R. Y., Suh, I., Zhao, J., Zhang, D., Fortner, E. C., Tie, X. X., et al., 2004. Atmospheric new particle formation enhanced by organic acids. Science. 304, 1487-1490.

Table 1 Summary of the reported atmospheric aerosol optical property measurement studies.

Country	Site	Period	b_{sca} (Mm^{-1})	b_{abs} (Mm^{-1})	SSA	Instruments	Reference
China	Shanghai	2009.12.23-2009.12.25	591 ± 143 (532 nm)	201 ± 51 (532 nm)	~ 0.75 (532 nm)	CRDS Nephelometer	Tang et al. (2014)
	Shanghai	2009.11.27-2009.12.06	332 ± 217 (532 nm)	85 ± 60 (532 nm)	0.48-0.86 (532 nm)	CRDS Nephelometer	Li et al. (2011)
	Shanghai	2010.04.02-2010.05.05	102 ± 75 (532 nm)	44 ± 35 (532 nm)	0.70 ± 0.07 (532 nm)	CRDS Nephelometer	Li et al. (2013)
	Beijing	2012.05.24-2012.06.22	/	/	~ 0.80 (550 nm)	CRDS Nephelometer Aethalometer	Li et al. (2017)
	Beijing	2005.01-2006.12	288 ± 281 (525 nm)	56 ± 49 (532 nm)	0.80 ± 0.09 (525 nm)	Aethalometer Nephelometer	He et al. (2009)
	Beijing	2006.08.11-2006.09.09	361 ± 295 (550 nm)	51.8 ± 36.5 (532 nm)	0.86 ± 0.07	PAS Nephelometer	Garland et al. (2009)
	Beijing	2005.03	468 ± 472 (550 nm)	65 ± 75 (550 nm)	0.81 - 0.85	PSAP Nephelometer	Li et al. (2007)
	Guangzhou	2004.10.05-2004.11.05	418 ± 195 (540 nm)	91 ± 60 (540 nm)	0.83 ± 0.05	PAS Nephelometer	Andreae et al. (2008)
Japan	Tokyo	2007.08.14-2007.09.02	130 ± 81.42 (532 nm)	13.6 ± 9.2 (532 nm)	0.89 ± 0.08 (532 nm)	CRDS PSAP Nephelometer	Nakayama et al. (2010)
USA	Pasadena	2010.05.30-2010.06.08	58 ± 43 (532 nm)	3.8 ± 3.4 (532 nm)	0.92 ± 0.08 (532 nm)	CRDS Nephelometer	Thompson et al. (2012)
European (Eastern Mediterranean)	Finokalia (Greece)	2001.03-2002.06	50 ± 23 (532 nm)	5.6 ± 3.6 (565 nm)	0.89 ± 0.04 (550 nm)	PSAP Nephelometer	Vrekoussis et al. (2005)
	Erdemli (Turkey)	1999.07-2000.06	90 ± 160 (532 nm)	/	/	Nephelometer	
	Finokalia, (Greece)	2001.06-2007.01	40.3 ± 27.1 (543 nm)	5.4 ± 3.7 (565 nm)	/	PSAP Nephelometer Aethalometer	Kalivitis et al. (2011)
European (Western Mediterranean)	Valencia (Spain)	2006.03-2010.12	80 ± 50 (550 nm)	/	/	Nephelometer	Esteve et al. (2012)

Table.2 Summary of the average and maximum values of b_{ext}, b_{sca}, b_{abs}, SSA, PM_{10}, O_3, NO, NO_2 and NO_x during the different period.

			b_{ext} (Mm^{-1})	b_{sca} (Mm^{-1})	b_{abs} (Mm^{-1})	SSA	PM_{10} ($\mu g/m^3$)	O_3 ($\mu g/m^3$)	NO ($\mu g/m^3$)	NO_2 ($\mu g/m^3$)	NO_x ($\mu g/m^3$)
Spring	All	Ave	65.6	54.9	10.6	0.81	30.6	66.3	1.2	5.7	6.8
		Std	67.8	58.2	10.9	0.10	21.6	23.9	4.1	4.2	6.2
		Max	317.8	256.0	68.3	1.00	93.4	137.8	79.7	25.8	95.0
	C-1	Ave	23.5	21.5	2.0	0.91	10.0	78.8	0.6	4.3	4.9
		Std	12.7	11.9	1.2	0.06	5.4	7.1	0.8	1.8	2.3
		Max	44.0	41.8	13.1	1.00	20.5	89.8	4.3	9.4	12.2
	P-1	Ave	164.8	140.4	24.4	0.85	62.1	67.3	1.3	6.3	7.6
		Std	54.3	46.9	11.0	0.05	15.0	21.7	4.0	3.3	4.7
		Max	317.8	256.0	68.3	1.00	93.4	110.0	35.4	21.3	41.2
	P-2	Ave	136.3	116.5	19.8	0.86	44.8	60.3	1.1	5.7	6.8
		Std	56.8	46.3	12.0	0.05	13.6	24.9	2.4	2.7	3.0
		Max	249.1	205.0	60.0	1.00	73.8	107.4	13.5	12.5	15.6
	C-2	Ave	10.1	8.1	2.0	0.81	11.7	77.8	0.3	2.9	3.1
		Std	8.1	4.3	4.7	0.11	6.8	10.0	0.4	1.0	1.0
		Max	191.9	74.3	131.1	1.00	43.9	92.6	2.0	5.2	5.5
	L-1	Ave	77.9	66.8	11.1	0.84	30.4	45.1	0.8	5.5	6.2
		Std	74.0	64.4	11.0	0.10	25.1	28.8	1.0	4.0	4.2
		Max	303.3	244.2	59.0	1.00	93.4	98.9	5.6	21.6	22.3

		Ave	37.5	35.4	3.9	0.83	17.4	37.0	15.3	34.4	49.7
	All	Std	37.8	36.7	4.4	0.13	11.8	20.4	13.0	11.6	20.9
		Max	251.2	221.8	53.2	1.00	77.5	87.2	130.7	84.5	197.4
		Ave	12.3	9.8	2.9	0.77	9.9	50.3	12.6	28.2	40.8
Autumn	C	Std	7.5	6.5	2.7	0.14	3.8	15.6	2.8	7.1	9.2
		Max	59.9	52.4	28.9	1.00	21.4	87.2	41.8	59.7	101.5
		Ave	52.7	50.5	4.8	0.88	22.0	28.8	17.4	39.4	56.8
	M	Std	40.5	38.7	5.3	0.10	12.7	18.6	17.0	12.1	24.6
		Max	251.2	221.8	53.2	1.00	77.5	74.6	130.7	84.5	197.4

Figure Captions

Fig. 1. Time series of b_{ext}, b_{sca}, b_{abs}, SSA at 532 nm, PM_{10}, O_3, NO, NO_2, NO_x, RH and T from: (a) 7 March to 25 April, (b) 25 October to 5 December 2013.

Fig. 2. Statistic diurnal variation of PM_{10}, Boundary layer depth (BLD), NO_x, O_3 and J_{NO2} from: (a) 7 March to 25 April, (b) 25 October to 5 December 2013.

Fig. 3. Statistic diurnal variation of b_{abs}, b_{sca} and SSA at 532 nm from: (a) 7 March to 25 April, (b) 25 October to 5 December 2013.

Fig. 4. The estimated fraction of photochemical reaction producing particles in PM_{10}.

Fig. 5. Statistic diurnal variation of the particle size distribution, NO_x, O_3 and J_{NO2} from 31 October to 9 November, 2013.

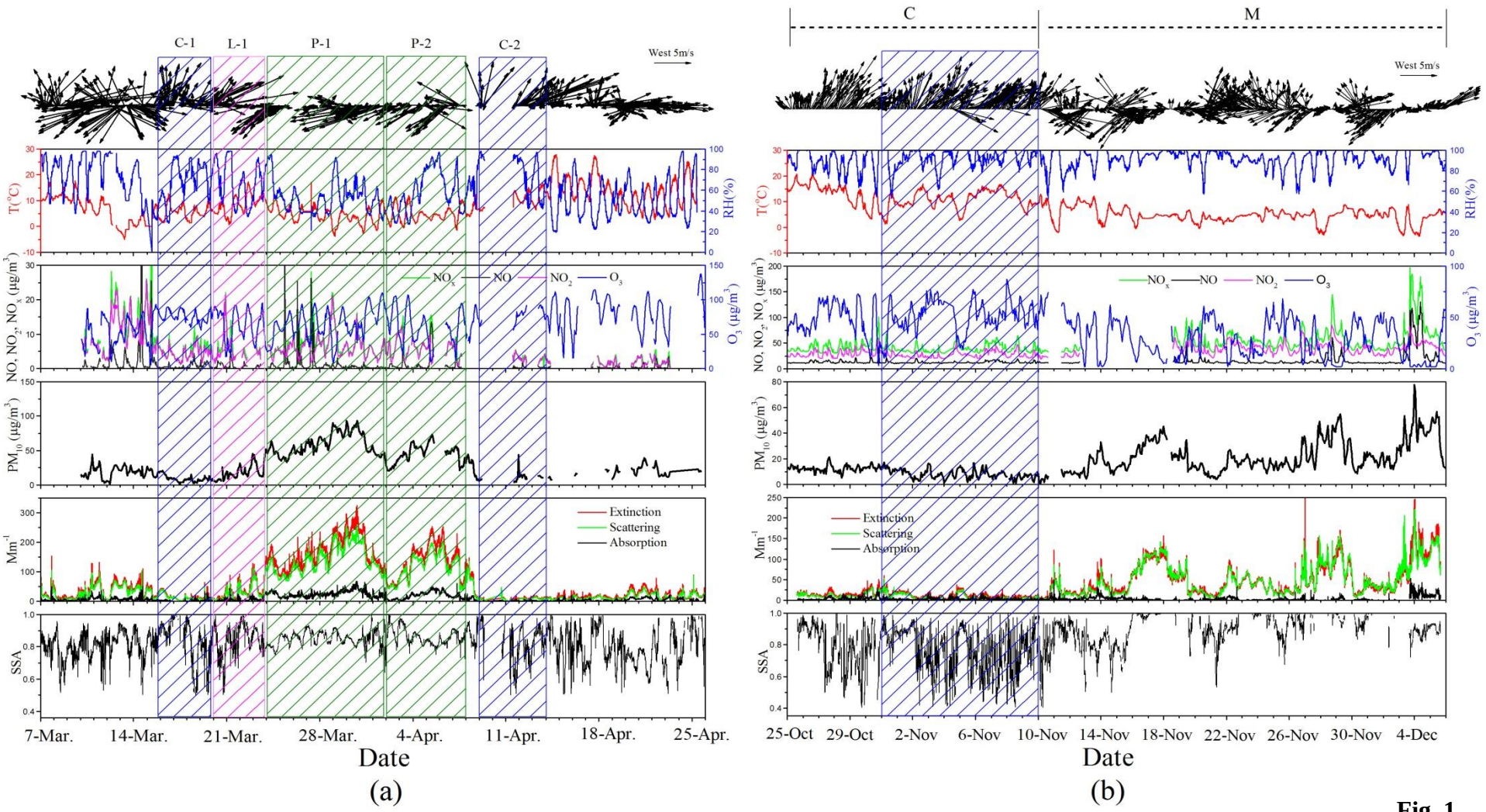

C-1
L-1
P-1
P-2
C-2
West 5m/s
T(°C)
RH(%)
NO, NO2, NOx (μg/m3)
O3 (μg/m3)
NOx
NO
NO2
O3
PM10 (μg/m3)
Mm-1
Extinction
Scattering
Absorption
SSA
7-Mar.
14-Mar.
21-Mar.
28-Mar.
4-Apr.
11-Apr.
18-Apr.
25-Apr.
Date
(a)
C
M
West 5m/s
25-Oct
29-Oct
2-Nov
6-Nov
10-Nov
14-Nov
18-Nov
22-Nov
26-Nov
30-Nov
4-Dec
Date
(b)

Fig. 1

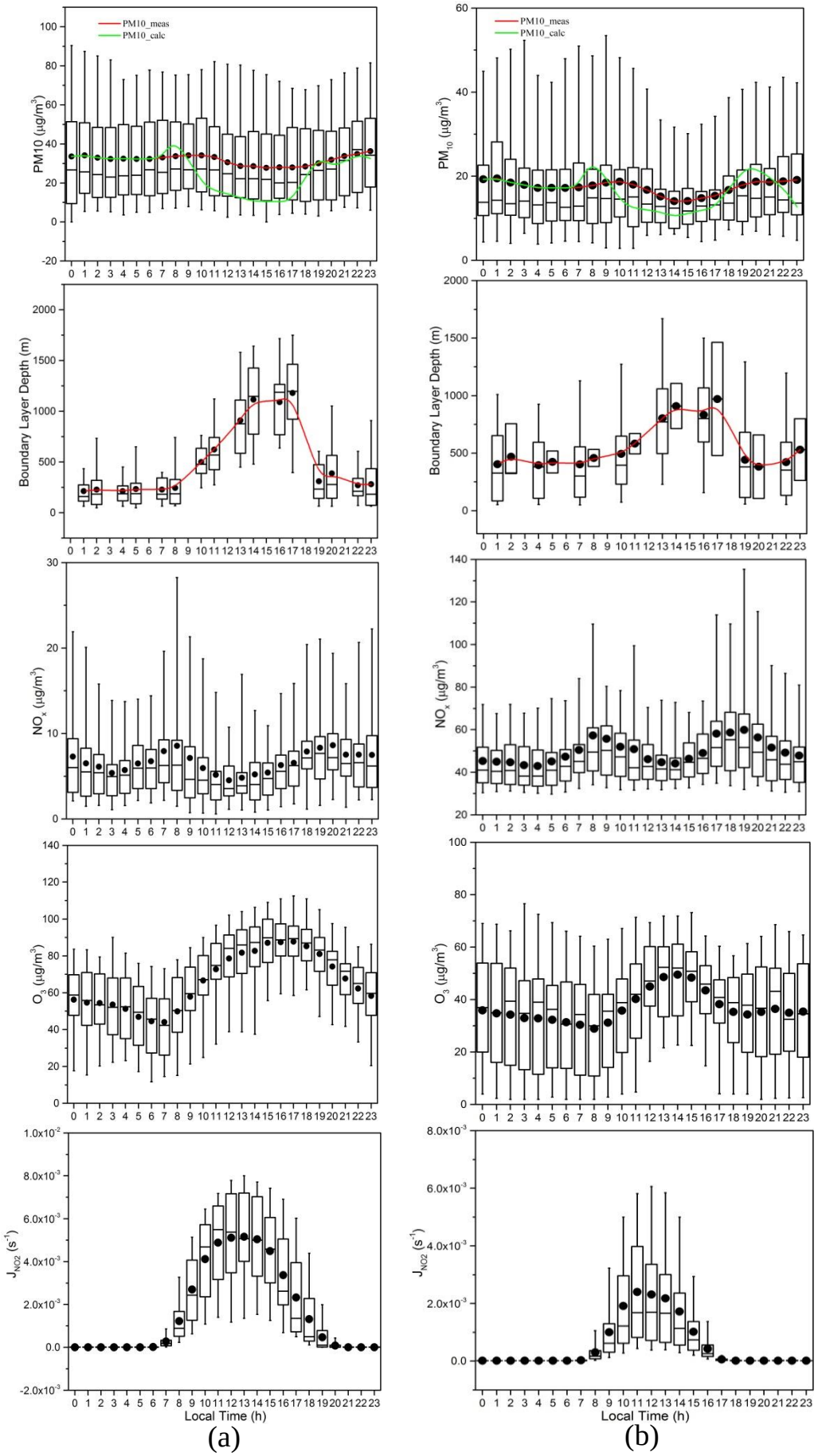

PM10_meas
PM10_calc
PM10 (μg/m³)
PM10 (μg/m³)
Boundary Layer Depth (m)
Boundary Layer Depth (m)
NOx (μg/m³)
NOx (μg/m³)
O3 (μg/m³)
O3 (μg/m³)
JNO2 (s-1)
JNO2 (s-1)
Local Time (h)
Local Time (h)
(a)
(b)

Fig. 2

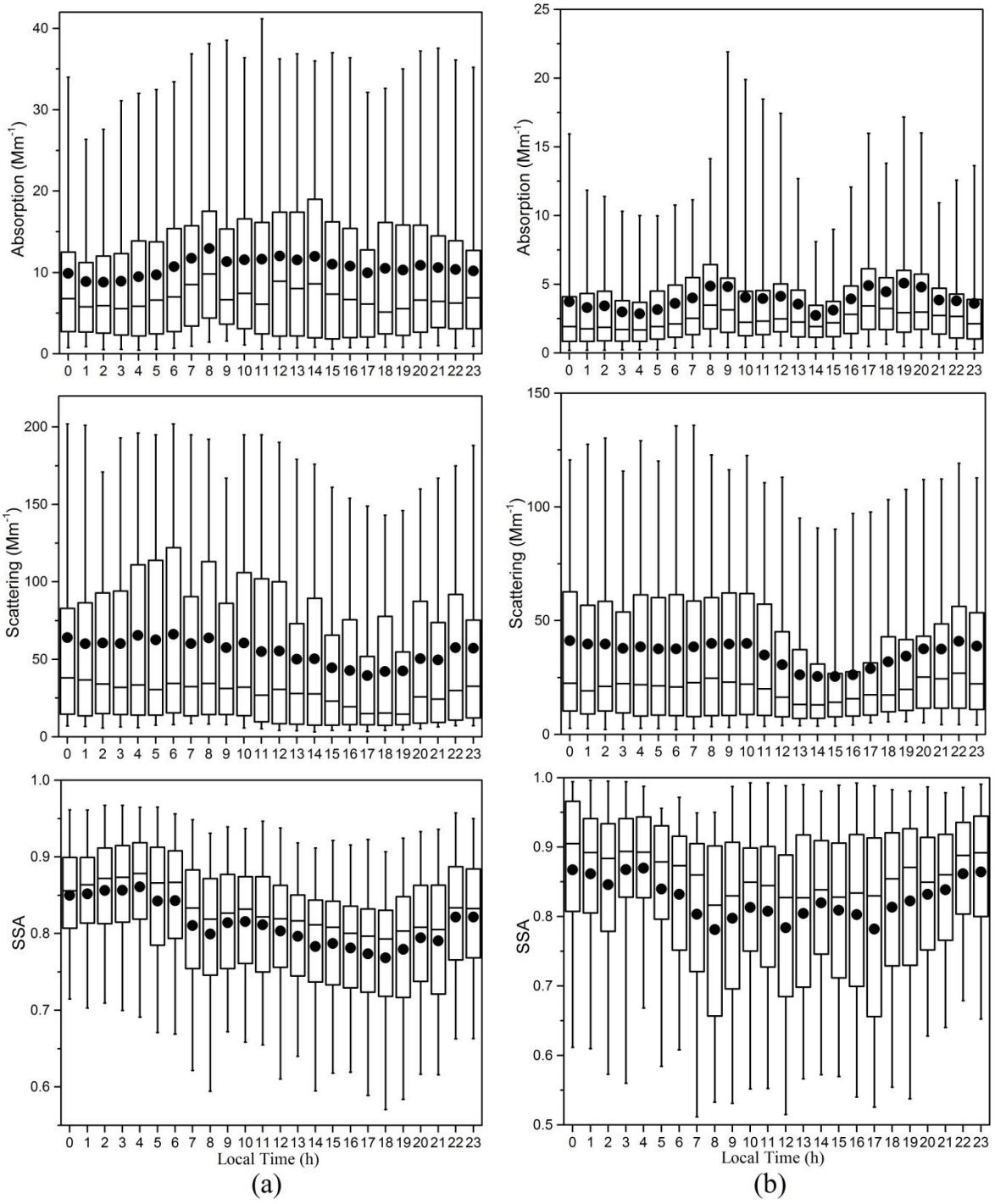


Fig.3

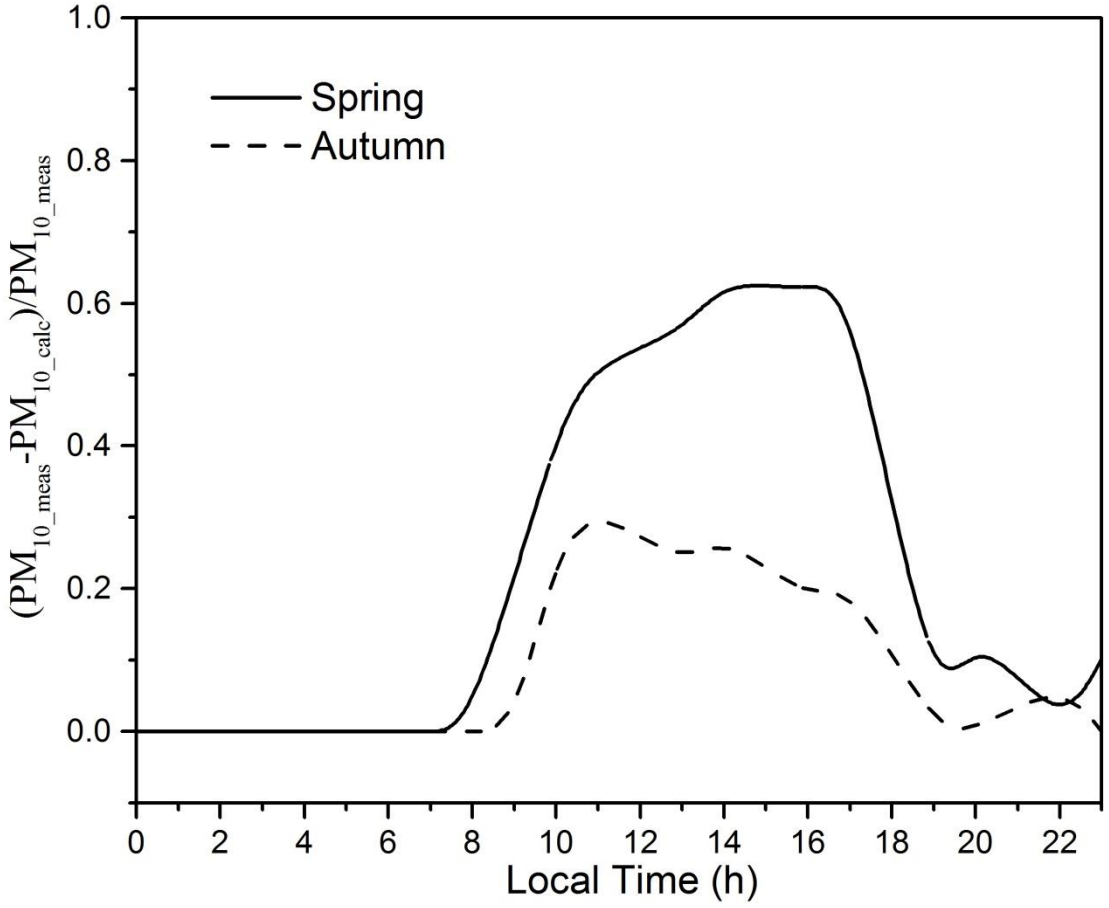

Spring
Autumn
(PM10_meas-PM10_calc)/PM10_meas
Local Time (h)
1.0
0.8
0.6
0.4
0.2
0.0
0
2
4
6
8
10
12
14
16
18
20
22

Fig.4

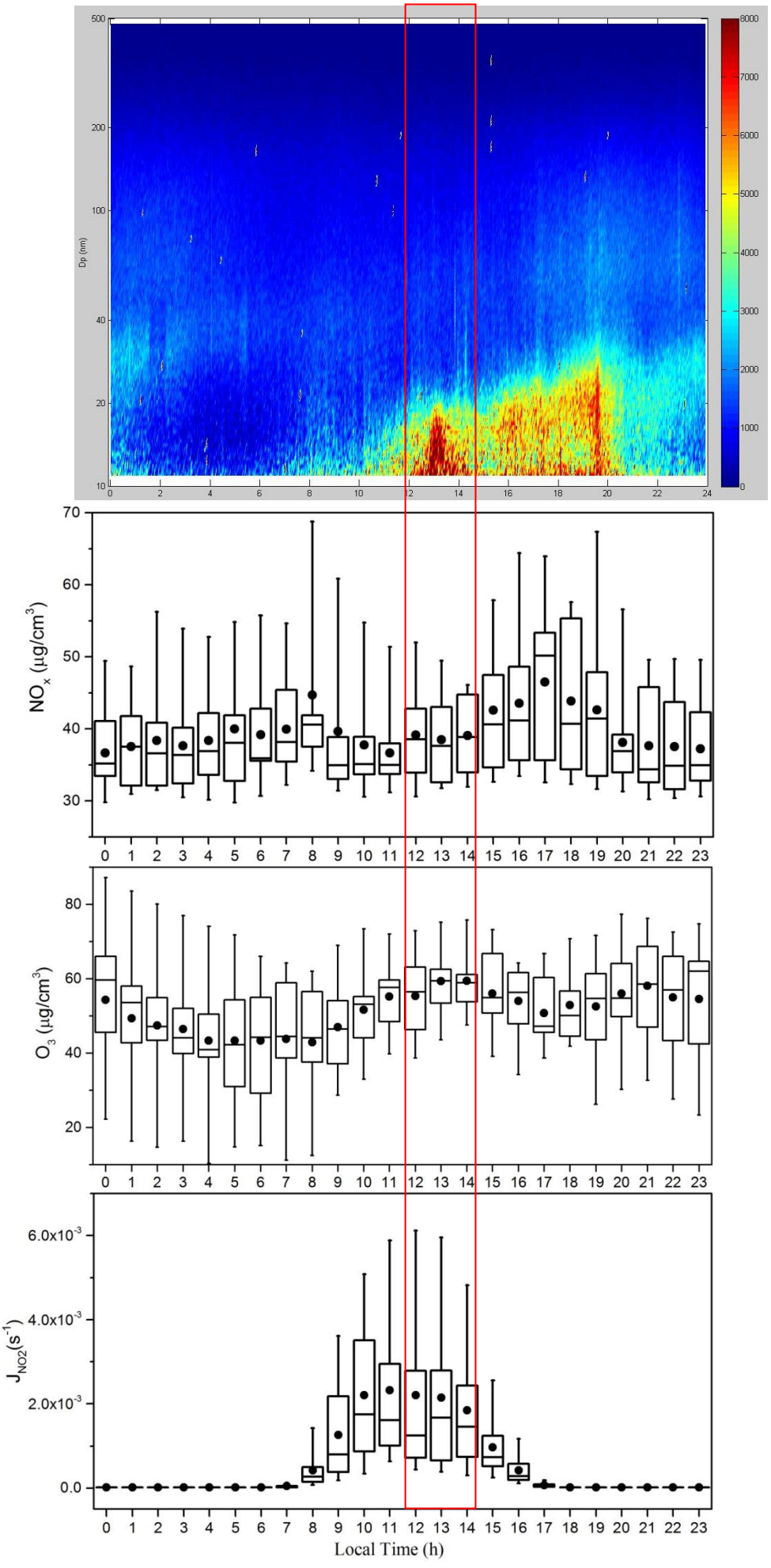

Dp (nm)
500
200
100
40
20
10
0 2 4 6 8 10 12 14 16 18 20 22 24
8000
7000
6000
5000
4000
3000
2000
1000
0
NO$_x$ (μg/cm^3)
70
60
50
40
30
0 1 2 3 4 5 6 7 8 9 10 11 12 13 14 15 16 17 18 19 20 21 22 23
O$_3$ (μg/cm^3)
80
60
40
20
0 1 2 3 4 5 6 7 8 9 10 11 12 13 14 15 16 17 18 19 20 21 22 23
J$_{NO2}$(s^{-1})
6.0x10^{-3}
4.0x10^{-3}
2.0x10^{-3}
0.0
0 1 2 3 4 5 6 7 8 9 10 11 12 13 14 15 16 17 18 19 20 21 22 23
Local Time (h)

Fig.5